Two-dimensional MR elastography with linear inversion reconstruction: methodology and noise analysis

Jonathan Bishop, Abbas Samani, Justin Sciarretta and Donald B Plewes†

Department of Medical Biophysics, University of Toronto, 2075 Bayview Avenue, North York, Ontario, M4N 3M5, Canada

E-mail: `dbp@srcl.sunnybrook.utoronto.ca`

Abstract. A methodology for imposing approximate plane strain conditions in magnetic resonance elastography through physical constraint is described. Under plane strain conditions, data acquisition and analysis may be conducted in two dimensions, which reduces imaging and reconstruction time significantly compared with three-dimensional analysis. Simulations and experiments are performed to illustrate the constraint concept. A signal/noise analysis of a two-dimensional linear inversion technique for relative elastic modulus is undertaken, and modifications to the numerical method are described which can reduce the SNR requirements by a factor of two to four. Experimentally measured data are reconstructed to illustrate the performance of the method.

1. Introduction

Contrast based on tissue elastic properties has significant potential for imaging breast cancer and other disease (Sarvazyan *et al* 1994). Since MR imaging is not directly sensitive to elastic modulus, such properties must be calculated from measurements of displacement. Displacement within an object is generated by either quasistatic or oscillatory stresses applied mechanically at the object surface, or remotely by other means such as ultrasound (Andreev *et al* 1997). In MRI, displacement is reliably measured with phase contrast methods (Pelc *et al* 1991). Thus the procedure of MR elastography (MRE) is composed of two distinct phases: acquisition of the displacement vector field through combined MRI and applied stress, followed by a data processing stage in which elastic modulus values and other variables may be calculated from raw displacement data (Ophir *et al* 1997).

Strain images represent a good method of displaying the results of MR elastography. They require only moderate SNR and can be computed promptly. For simple geometries such as focal masses, strain is related linearly to elastic modulus (Plewes *et al* 2000), and may suffice as a reconstruction method. In situations where more accurate modulus depiction is required, a calculation of the modulus based on governing partial differential equations and known boundary conditions may be performed. This calculation is ill-conditioned, and thus SNR requirements are high and the computation time is significant. Nevertheless, a number of investigators have pursued this approach with their displacement data (Skovoroda *et al* 1995,

† Author to whom correspondence should be addressed at: Department of Medical Biophysics, Imaging/Bioengineering Research Group, Sunnybrook and Women's College Healths Sciences Centre, 2075 Bayview Avenue Toronto, Ontario Canada M4N 3M5.

Chenevert *et al* 1998, Kallel and Bertrand 1996, Manduca *et al* 1996, Dutt *et al* 1997, Sinkus *et al* 1999, Weaver *et al* 1999).

In this paper, we review previous inverse methods employed in MRE, and then focus on the linear inversion approach with a signal/noise analysis, and modifications for improved noise performance. We also describe a strategy for MR elastography that applies physical constraints to create an approximate state of plane strain in the object. Under plane strain, it is possible to perform accurate modulus reconstruction on two-dimensional strain data; this represents large potential savings in data acquisition and reconstruction time compared with the alternative of making three-dimensional strain measurements.

1.1. Inverse methods for elastography

The Navier vector equation is derived from Hooke's law, Newton's law and the continuum hypothesis (Chandrasekharaiah and Debnath 1994). In the following simplified form, it governs deformations in linear, isotropic elastic materials:

$$\nabla(\lambda \nabla \cdot \boldsymbol{u}) + \mu(\nabla^2 \boldsymbol{u} + \nabla \nabla \cdot \boldsymbol{u}) + (\nabla \mu)(\nabla \boldsymbol{u} + \nabla \boldsymbol{u}^T) = \gamma \frac{\partial \boldsymbol{u}}{\partial t} + \rho \frac{\partial \boldsymbol{u}}{\partial t^2} \qquad (1)$$

where λ is a Lamé constant, μ the shear modulus and $\boldsymbol{u}$ is the displacement vector field. On the right-hand side, γ and ρ are the material parameters of viscous damping and density respectively. Depending on whether or not the data are acquired under dynamic loading conditions, the right-hand side may be omitted. In MRE, the shear modulus μ is the primary unknown of interest. Although the Lamé constant λ is also unknown, it can be eliminated by several means as described below.

There are two basic approaches to solving (1) numerically for modulus μ. If the equation is discretized directly with modulus as the unknown, it may be solved with standard linear algorithms (Hansen *et al* 1998). This requires boundary conditions in terms of the unknown elastic modulus, although it may be sufficient to assume a constant boundary modulus to achieve a relative modulus reconstruction. Alternatively, (1) may be solved in the usual forward sense with displacement as the unknown, based on a current estimate of modulus. The modulus estimate is updated through some nonlinear algorithm and the process repeated iteratively until the calculated displacement converges to experimentally measured displacement (Kallel and Bertrand 1996, Bishop and Plewes 1998). In this approach, exact displacement boundary conditions are available from the experimental data. In either case, most inversion methods published to date (Skovoroda *et al* 1995, Chenevert *et al* 1998, Kallel and Bertrand 1996, Manduca *et al* 1996, Dutt *et al* 1997, Weaver *et al* 1999) have assumed linear elasticity, small-strain deformation and two-dimensional plane strain conditions. These assumptions limit the number of unknown variables and spatial locations such that the resulting matrix equation may be solved with a desktop workstation in a reasonable amount of time.

Skovoroda *et al* (1995) were the first to describe inverse calculations of elastography data, using a direct linear inversion of (1). Assuming tissue incompressibility, $\lambda \nabla \cdot \boldsymbol{u}$ is indeterminate and was therefore eliminated analytically by taking another partial derivative. In two dimensions, equation (1) thus reduces to a scalar equation involving a single (unknown) modulus quantity (μ) and two (known) displacement components (u_1, u_2). Phantom results were shown for a 20×20 (4 mm^2 pixel) grid, 5 mm deformation and low-contrast modulus ratio <2. Chenevert *et al* have applied the Skovoroda method to static MR displacement data (Chenevert *et al* 1998). Results were shown in phantoms and *ex vivo* kidney encased in gel for a 128×128 grid and 1.5 mm compression. More recently, the method was extended to account for nonlinear effects, and an integral formalism introduced for improved performance with noisy data (Skovoroda *et al* 1999).

Kallel has presented a nonlinear iterative solution for static ultrasound data (Kallel and Bertrand 1996). In that approach, (1) is expressed using Poisson's ratio in place of Lamé constant λ:

$$\lambda = \frac{2\mu\nu}{1 - 2\nu} \tag{2}$$

and a near-incompressible value of $\nu = 0.495$ is assigned for all tissues, leaving only modulus μ as a single unknown. A Gauss–Newton algorithm was used to solve the least-squared error minimization problem

$$\min ||\boldsymbol{u}(\mu) - \boldsymbol{u}_m||^2 \tag{3}$$

in an iterative fashion. Here, $\boldsymbol{u}_m$ represents the experimentally measured displacement data, and $\boldsymbol{u}(\mu)$ represents the calculated displacement from the current estimate of modulus. Results were shown in simulated data with and without noise for a 25×25 grid, 0.5 mm compression, and low-contrast modulus ratio of 3.

Ehman *et al* have presented two inversion methods to analyse dynamic shear wave MR data. Initially, modulus is inferred through estimation of local wavelength (Manduca *et al* 1996). The resolution of this method is related to the shear wavelength, but it is straightforward to implement. As an extension of this method, equation (1) was expressed as an inverse scattering problem and solved iteratively (Dutt *et al* 1997). Results were presented for noise-free simulated data on a 128×128 grid (1 mm^2), and low modulus contrast <3.

Recently, Sinkus *et al* (1999) and Weaver *et al* (1999) analysed MR elastography data with a steady-state harmonic model where the displacement $\boldsymbol{u} = \boldsymbol{U}\mathrm{e}^{\mathrm{i}\omega t}$:

$$\nabla(\lambda\nabla \cdot \boldsymbol{U}) + \mu(\nabla^2\boldsymbol{U} + \nabla\nabla \cdot \boldsymbol{U}) + \nabla\mu(\nabla\boldsymbol{U} + \nabla\boldsymbol{U}^T) = -\omega\gamma\boldsymbol{U} + \omega^2\rho\boldsymbol{U}. \tag{4}$$

Weaver solved this equation with the Poisson's ratio approximation (equation (2), $\nu = 0.49$) and an iterated Gauss–Newton method. As a further refinement to break down the computational load, the reconstruction field of view was subdivided into smaller regions of interest, solved in parallel, and reassembled. Sinkus *et al* were the first to produce a three-dimensional reconstruction from 3D displacement data. Using the Poisson's ratio approximation and assuming that modulus is locally constant ($\nabla\mu = 0$):

$$\frac{E}{2(1 + \nu)}\nabla^2\boldsymbol{U} + \frac{E}{2(1 + \nu)(1 - 2\nu)}\nabla\nabla\boldsymbol{U} = -\omega\gamma\boldsymbol{U} + \omega^2\rho\boldsymbol{U} \tag{5}$$

thereby converting the boundary value problem to a pixel-by-pixel calculation.

Finally, Plewes *et al* (2000) have described an iterative approach that is highly constrained through use of *a priori* knowledge of the lesion geometry. This method is ideal for assessing focal masses where the inclusion can be segmented from normal tissue along a discrete boundary. It is computationally efficient in that the modulus update calculation is performed on a pixel-by-pixel basis as in Sinkus *et al* (1999), rather than solving a system of simultaneous equations as in Kallel and Bertrand (1996) or Weaver *et al* (1999).

In the following section, we describe modifications to the linear inversion technique of Skovoroda *et al* (1995) in the handling of the Lamé constant λ, and in the use of regularization. These modifications are then shown to reduce the SNR requirements in the displacement data.

2. Theory

Plane strain conditions are often used to describe a cross-sectional state of stress in an object which is very long. It is assumed that motion in the long dimension is negligible compared with motion in the cross-sectional dimensions. Thus, a state of symmetry can be employed to make

approximate solutions in two dimensions. Most previous discussions of inverse problems in MR elastography assume plane strain conditions, but it is noted that such approximations are not very accurate for spherical inclusions (Bilgen and Insana 1998). However, an approximate state of plane strain can be achieved by simply constraining the material in one dimension, as shown below. The rest of this section assumes two-dimensional plane strain.

In incompressible materials such as soft tissue, the term $\lambda \nabla \cdot \boldsymbol{u}$ in (1) is indeterminate. It can be replaced by a variable p which is interpreted as the average pressure-stress. The vector equation describing static equilibrium in a linearly elastic material is thus:

$$\nabla p + \mu(\nabla^2 \boldsymbol{u} + \nabla \nabla \cdot \boldsymbol{u}) + (\nabla \mu)(\nabla \boldsymbol{u} + \nabla \boldsymbol{u}^T) = 0. \tag{6}$$

Using finite difference discretization of (6), a matrix equation can be assembled:

$$Kx = b, \qquad x = \{\mu_1, \mu_2, \ldots \mu_n, p_1, p_2, \ldots, p_n\}^T \tag{7}$$

where x is the solution vector, K is a $2n \times 2n$ matrix of displacement derivatives (stiffness matrix) and b is the right-hand side vector containing boundary condition information. Alternatively, pressure may be eliminated from (6) analytically, with the use of a third differential operation, as shown by Chenevert *et al* (1998). However, we retain p as an unknown, such that derivatives of the displacement vector field are limited to second order; this improves the conditioning of the stiffness matrix K. Furthermore, K has a 2×2 block structure of $n \times n$ submatrices K_{ij}:

$$K = \begin{pmatrix} K_{11} & K_{12} \\ K_{21} & K_{22} \end{pmatrix} \tag{8}$$

which can be utilized to optionally rewrite (7) as an $n \times n$ matrix equation $K'x = b'$ with:

$$K' = K_{11} - K_{12} \cdot K_{22}^{-1} \cdot K_{21}, \qquad b' = b_1 - K_{12} \cdot K_{22}^{-1} \cdot b_2 \tag{9}$$

whereby solution x is now an $n \times 1$ vector containing only the modulus variables μ_i. The elimination of pressure has been achieved through matrix partitioning rather than partial differentiation. The matrix partitioning operation is reliable because there are no displacement terms in the coefficient of the ∇p term. Therefore, K_{22} is a noise-free orthogonal matrix and the inverse is trivial to compute.

Tikhonov regularization (Hansen *et al* 1998) is formulated by the problem:

$$\min\{||Kx - b||^2 + \eta^2 ||L(x - x_0)||^2\} \tag{10}$$

where η is the regularization parameter, L is a Laplacian smoothing operator and x_0 is an initial solution guess. Depending on the value of η, the solution is biased towards greater smoothness and away from the actual data in matrix K. The solution is:

$$x_{L,\eta} = (K^T K + \eta^2 L^T L)^{-1}(K^T b + \eta^2 L^T x_0) \tag{11}$$

and can be expressed in terms of the generalized singular value decomposition (GSVD) of the matrices K, L in such a way that solutions for multiple values of η are efficiently computed with matrix multiplication operations (Golub and van Loan 1996).

In the following sections, three variants of the stiffness matrix K are analysed, and will be denoted as follows. $K2$ refers to the stiffness matrix of equation (7) with two solution variables and size $2n \times 2n$. $K2'$ refers to the stiffness matrix of equation (9) with one solution variable and size $n \times n$. Finally, $K1$ refers to the stiffness matrix of Chenevert *et al* (1998) where pressure has been eliminated analytically, with one solution variable and size $n \times n$.
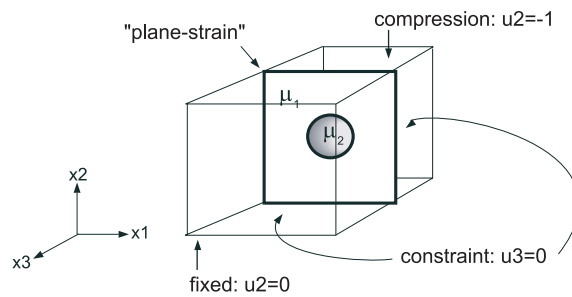
Figure 1. The model object used in three-dimensional simulations was a cube (thin solid lines) with a spherical inclusion (shaded). The object was discretized on a $48 \times 48 \times 48$ grid, and compression was simulated with a constraint (arrows) in the x_3 direction. The model object used in two-dimensional linear inversion calculations corresponds to the central x_1, x_2 plane of the three-dimensional object, as outlined in the thick solid lines. The 2D object was discretized on a 32×32 grid.
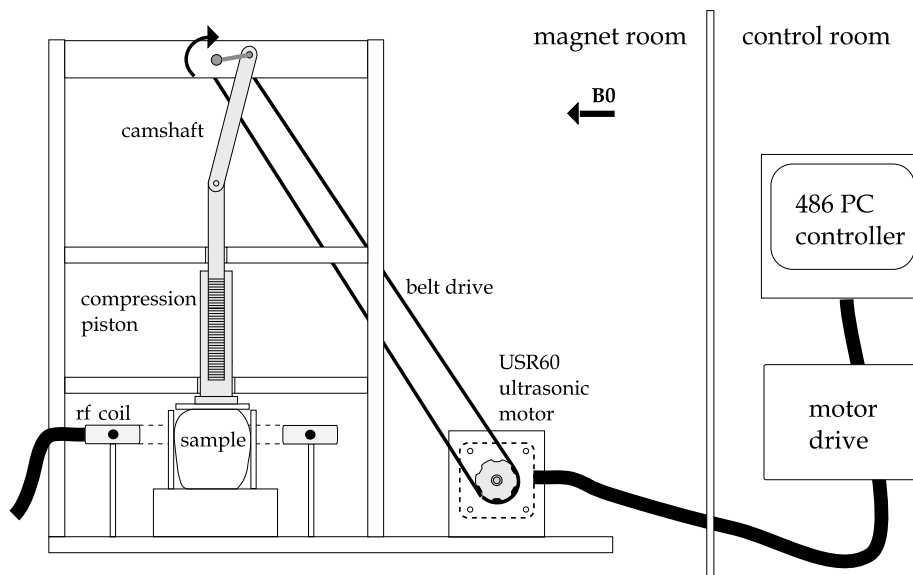
Figure 2. Experimental apparatus used to apply quasistatic deformation to test objects in the bore of the magnet. The sinusoidal motion of the compressor is achieved through a camshaft driven by a rotary ultrasonic motor at 1–2 Hz. Two vertical plates are shown constraining the sample from displacing in the horizontal direction, while the sample is free to deform in the direction perpendicular to the page.
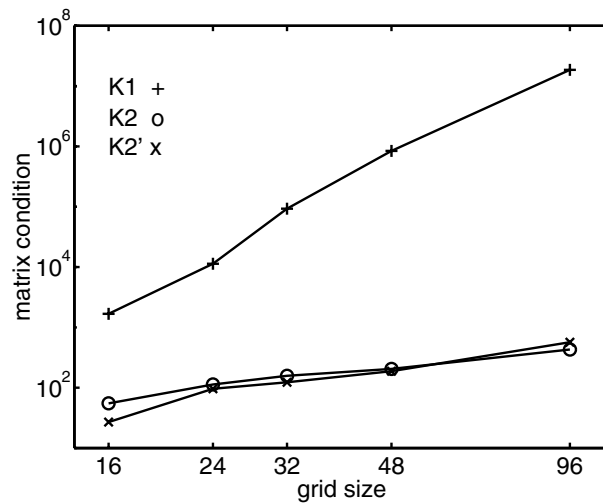
3. Methods

Simulations and experiments were initially conducted to demonstrate that plane-strain conditions can be achieved in a three-dimensional object through use of physical constraints. A three-dimensional inclusion object was simulated with a $48 \times 48 \times 48$ mesh (figure 1). A compression of 5% was simulated with zero-displacement constraints applied at the x_3 direction boundaries. The experimental three-dimensional inclusion phantom was constructed from plastisol PVC (M-F Manufacturing Company, Fort Worth, TX), having an inclusion
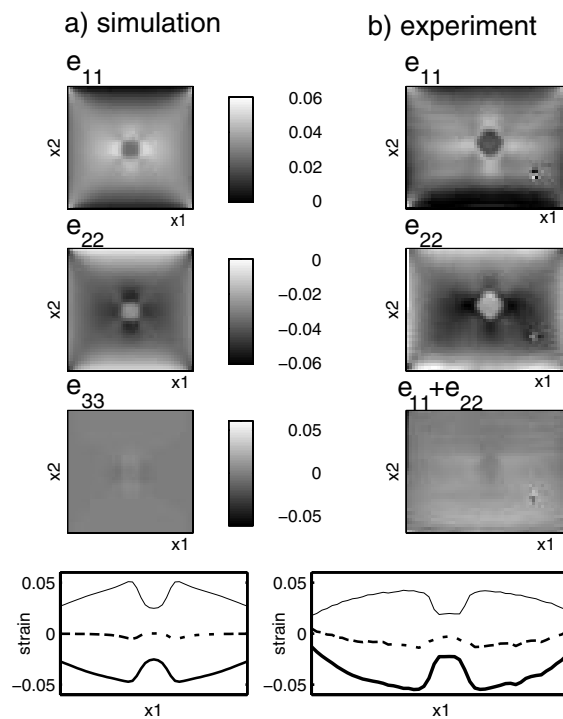
Figure 3. Simulated and experimental strains in a three-dimensional inclusion object. (*a*) Simulated results are shown for strain components e_{11}, e_{22}, and e_{33}. The strain in the restricted direction (e_{33}) is near zero. The bottom graph shows horizontal (x_1) profile plots of e_{11} (——), e_{22} (——) and e_{33} (– – –). (*b*) Experimental results for strain components e_{11}, e_{22} and $e_{11} + e_{22}$. The bottom graph shows horizontal (x_1) profile plots of e_{11} (——), e_{22} (——), and $e_{11} + e_{22}$ (– – –) which are qualitatively very similar to simulation. The aspect ratio is slightly different because the phantom was rectangular while the simulation was square.

modulus of 25.7 kPa and an exterior modulus of 11.9 kPa, as measured independently with benchtop apparatus. The phantom was placed in an MR-compatible compressor device driven by ultrasonic motor (USR60-N4, Shinsei Corp., Tokyo Japan) as illustrated in figure 2. Side panels were positioned to constrain this object in the x_3 direction (i.e. left/right in figure 2), and the motion measured in orthogonal directions with a stimulated-echo phase contrast method (Chenevert *et al* 1998). Imaging parameters used were $T_{\text{mix}} = 100$ ms, TE = 12.4 ms, two signal acquisitions, 64×64 matrix in a 9 cm field of view, and 4 mm slice thickness. The imaging sequence was prospectively gated to the sinusoidal motion signal, which had a period of 660 ms and an amplitude of 4 mm.

The linear inversion was evaluated with simulated data in two-dimensional plane strain to compare the three different discretization methods ($K1$, $K2$, $K2'$). The model geometry had a circular inclusion within a square field of view, denoted by heavy lines in figure 1. The sharp transition in modulus distribution was smoothed slightly with a 5×5 Gaussian convolution filter having a full-width half-maximum of 2.2 pixels. This smoothing is required because the finite difference approximations which are made in assembling equation (7) are first-order central differences, meaning that sharp discontinuities cannot be properly reconstructed. A finite element numerical method (Abaqus v5.8.1, HKS Inc.) was used to generate displacement data from this geometry corresponding to a strain of 5%. Normally distributed noise was added

Figure 4. The stiffness matrix condition number for each of the discretization methods ($K1$, $K2$, $K2'$) is plotted as a function of grid size. The grid size is the number of discrete nodes per spatial dimension. All subsequent inversions used a grid size of 32×32.

to the displacement vector to establish a signal/noise ratio in the displacement data that would correspond to experimentally measured data. Since displacement varies throughout the field of view in quasistatic elastography, the displacement SNR is quoted as the ratio of maximum displacement at the object surface to standard deviation of the noise. These noisy displacement data then became the input to the inverse calculation. The computing time for the GSVD of the matrices K, L is proportional to n^3, and took about 90 min on a Sun Ultra 10 workstation for the $K2$ matrix on a 32×32 grid.

Two theoretical methods of selecting η were initially studied. The discrepancy principle (Morozov 1984), which balances the residual norm ($\parallel Kx - b \parallel_2$) against the noise in b, tended to oversmooth the result in the simulations. Furthermore, the noise in b may not be precisely known in experimental data, so this method was discarded. L-curve analysis (Hansen *et al* 1998), which balances the residual norm against the smoothing norm ($\parallel Lx \parallel_2$) yielded good results for very high SNR. With the lower SNR values selected in this study, the L-curve approach was also unsuccessful. Consequently, the 'best' value of η was difficult to define in a numerical fashion. Instead, 14 trial solutions were generated with η values ranging over two orders of magnitude. The value of η was determined empirically from that solution which presented a reasonable balance between numerical artefact and over-smoothing of the inclusion. The trial solutions required only a few minutes to generate once the GSVD of the matrices K, L was available. Typical values of η ranged between 0.05 and 0.1 for the various simulations in this study. In addition, the experimentally measured displacement data were processed with the $K2$ discretization.

4. Results

Figure 3 presents simulated and experimental results for compression of a three-dimensional object under lateral constraint. In the simulation (figure 3(a)), the strain component corresponding to the constrained direction (e_{33}) shows that a good state of plane strain is achieved. The experimental results (figure 3(b)) show the strain components measured

a) K2: μ   **b) SNR 1000**
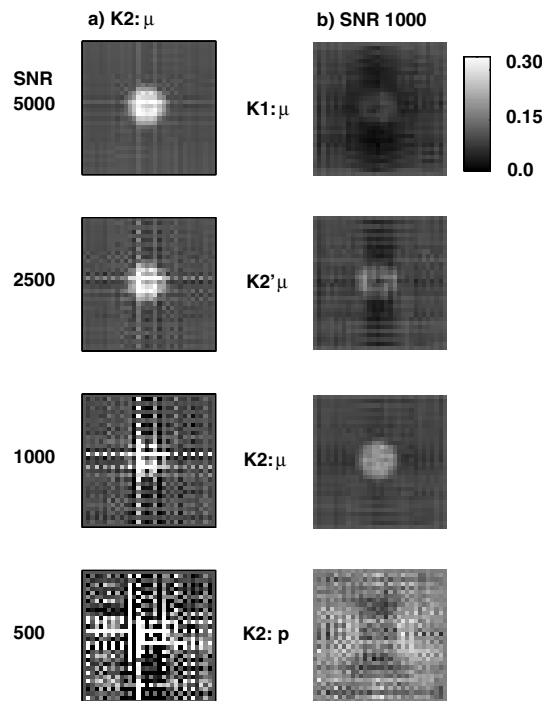
Figure 5. Linear inversion reconstruction results are shown for various SNR levels in the simulated displacement data. All images are displayed with the same colourmap. (*a*) The left column of images shows the modulus reconstruction by LU decomposition (unregularized) from the *K*2 discretization. As the SNR level decreases below 1000, the solution rapidly diverges. (*b*) The right column shows the regularized modulus reconstruction for each discretization and SNR = 1000, as well as the *K*2 pressure reconstruction. The regularization parameters were 0.05, 0.1 and 0.06 for *K*1, *K*2′, *K*2 respectively.

in the two unconstrained dimensions e_{11} and e_{22}. The component e_{33} was not measured experimentally so the sum $e_{11} + e_{22}$ is shown in comparison with the component e_{33} of the simulation. A horizontal profile of $e_{11} + e_{22}$ demonstrates that $e_{11} \simeq -e_{22}$. Since the Poisson's ratio of plastisol is >0.499 (Erkamp *et al* 1998), the trace of the strain tensor should be zero, and thus it is concluded that there is virtually no strain in the x_3 direction.

The stiffness matrix K can be characterized by the condition number, which is a measure of the sensitivity to perturbations in the displacement data such as noise or discretization errors (Golub and van Loan 1996). In figure 4, the matrix condition is plotted for each discretization method: combined pressure/modulus ($K2$), modulus only by matrix partitioning ($K2'$) and modulus only by partial differentiation ($K1$). The grid size is the number of discrete nodes per spatial dimension. As the relative degree of perturbation approaches the reciprocal of the condition number, the LU decomposition solution to equation (7) will typically begin to diverge. The graph in figure 4 shows the relative advantage in matrix conditioning in $K2$ and $K2'$ where calculation of the third spatial derivative of displacement has been avoided.

Figure 5 shows results for the linear inversions on simulated two-dimensional data. In the left column (figure 5(*a*)), the LU decomposition (unregularized) modulus reconstruction of the $K2$ stiffness matrix is shown for various displacement SNR between 500 and 5000. The solution diverges for SNR below 1000. In the right column (figure 5(*b*)), the regularized solution for each of the three discretizations ($K1$, $K2$, $K2'$) is presented for SNR = 1000.
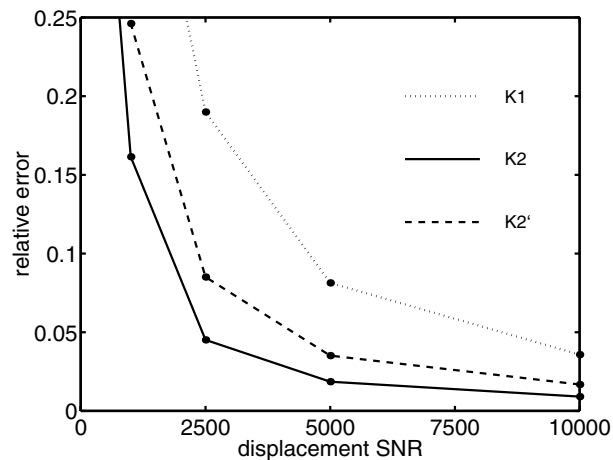
Figure 6. RMS error for the regularized modulus reconstruction by each discretization method ($K1$, $K2$, $K2'$) is plotted as a function of the displacement SNR. Data points (circles) are connected by straight lines for qualitative comparison.

The effect of regularization may be directly compared on the third row of the figure, where the $K2$ modulus reconstruction is presented with and without regularization. Although much artefact is removed by the regularization, there is clearly some attenuation of the modulus as well, so SNR $= 1000$ can be interpreted as a bare minimum requirement. The regularized modulus reconstruction for $K2'$ is somewhat worse than for $K2$, and the inclusion can just be detected in the $K1$ reconstruction. The pressure reconstruction from the $K2$ matrix is noisy and of less intrinsic interest, except as a means of obtaining a better modulus reconstruction.

Figure 6 plots the rms error in the modulus reconstruction returned by the three methods of discretization. Depending on the tolerance on this reconstruction error, the $K2$ and $K2'$ discretization methods offer from two to four times reduction in required SNR for an equivalent level of reconstruction error. Figure 7 illustrates the $K2$ modulus reconstruction of the experimental data in figure 3. The magnitude image (figure 7(*a*)) shows a relatively good SNR of about 60. There are approximately two cycles of phase wrap in the data, so the corresponding displacement SNR is roughly $2 \times 2\pi \times 60 = 750$. The noise was further reduced by 50% using a 9×9 Gaussian convolution filter of full-width half-maximum 1.5 pixels prior to reconstruction. In addition to reducing noise, this filter also smooths the discontinuity in the displacement data due to the sharp boundary of the inclusion, as required for central difference approximation of differentiation. The regularized modulus reconstruction is shown as a value relative to 1 in the background region of the phantom (figure 7(*b*)). Figure 7(*c*) shows a line profile of the reconstructed modulus, and a simulated profile corresponding to the benchtop measurements of elastic modulus in the separate material components of the phantom.

5. Conclusions

In direct linear inversion of MR elastography data, SNR requirements are fairly high due to the ill-conditioning of the inversion equations. We have described the benefits of solving for pressure simultaneously with elastic modulus in a linear inversion procedure. Retaining pressure as an unknown has the advantage of improving the conditioning of the numerical problem, but it carries an additional computational expense of roughly a factor of eight.
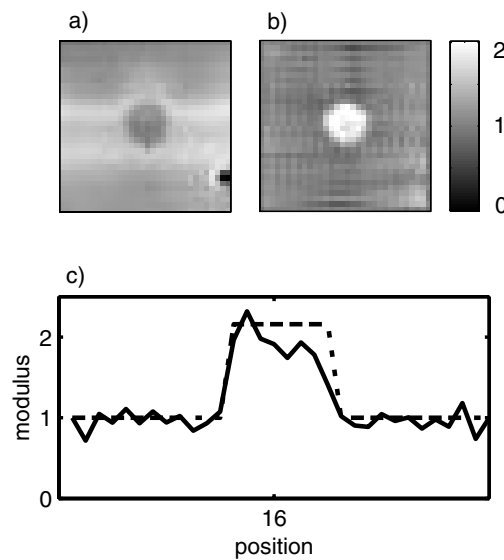
Figure 7. (*a*) A 32 × 32 region of interest in the magnitude image of the three-dimensional inclusion phantom shows relatively high SNR of 60. The inclusion appears dark, due to a shorter T2 relaxation time. The dark area at bottom right is an air bubble. (*b*) Relative modulus reconstruction of experimental data from $K2$ discretization on a 32 × 32 grid. (*c*) Line profile of reconstructed modulus (solid line) compared with the true modulus of the phantom as measured separately on benchtop apparatus (dashed line).

If matrix partitioning (rather than partial differentiation) is used to eliminate the pressure term, a good compromise is obtained whereby computation time is not affected, but some noise tolerance is gained. The decrease in SNR that can be tolerated by using the $K2$ or $K2'$ discretizations ranges from two to four. The recent integral formulation of the $K1$ discretization (Skovoroda *et al* 1999) is also designed to address this noise sensitivity.

Many investigators have identified the goal of solving a three-dimensional modulus distribution with accompanying 3D displacement data set. However, even a low-resolution 3D reconstruction is a challenging numerical problem and data acquisition requirements are substantial (Chenevert *et al* 1999). As an alternative, we have demonstrated with phantoms made of incompressible materials that confinement techniques may be used to effectively produce plane-strain conditions, such that measurement and analysis can be conducted in two dimensions.

The sensitivity to perturbation in the inversion equations means that filtering must be considered for two purposes. If the displacement SNR is low, then the noise must be reduced to obtain SNR > 1000. If the SNR is high, some filtering must still be applied to eliminate discontinuities which cannot be reconstructed by low-order finite difference approximations. It is possible to use finite difference approximations corresponding to higher-order interpolating polynomials, but if it is known in advance that some low-pass filtering will be required to deal with noise in the data, then first-order approximations are sufficient. While the requirement of SNR > 1000 is high, we have recently demonstrated *in vivo* displacement SNR of 300 in parenchymal tissue (Plewes *et al* 2000). In that procedure, two components of displacement were obtained in one slice location during four minutes of scan time. Improvements to our phased array detector, combined with the option of increasing the relatively brief scan time, should be sufficient to obtain a displacement SNR of 1000 *in vivo*. Nevertheless, the linear inversion is a demanding problem and may ultimately be inappropriate for use *in vivo*; Plewes *et al* (2000) also contains a discussion of a more robust reconstruction methodology.

In the context of breast MRI, it can be assumed that lesion detection is accomplished with Gd-DTPA enhanced 3D MRI. Elastography must only help classify a particular lesion as benign or malignant. Thus, reconstruction is only required on a localized ROI surrounding a specific lesion of interest, which greatly simplifies the numerical complexity of the problem, as originally noted in Skovoroda *et al* (1994). The 32×32 grid described above is representative of the size required for a localized reconstruction.

Acknowledgments

References

Andreev V, Dmitriev F, Pishchal'nikov Y, Rudenko O, Sapozhnikov O and Sarvazyan A 1997 Observation of shear waves excited by focused ultrasound in a rubber-like medium *Acoust. Phys.* **43** 123–8

Bilgen M and Insana M 1998 Elastostatics of a spherical inclusion in homogeneous biological media *Phys. Med. Biol.* **43** 1–20

Bishop J and Plewes D 1998 An alternate method for calculating elastic properties of breast tissue *Proc. Sixth Meeting of the ISMRM (Sydney)* p 2102

Chandrasekharaiah D and Debnath L 1994 *Continuum Mechanics* (New York: Academic)

Chenevert T, Skovoroda A, O'Donnell M and Emelianov S 1998 Elasticity reconstructive imaging by means of stimulated echo MRI *Magn. Reson. Med.* **39** 482–90

Dutt V, Manduca A, Muthupillai R, Ehman R and Greenleaf J 1997 Inverse approach to elasticity reconstruction in shear wave imaging *IEEE Int. Ultrasonics Symp., Program and Abstracts* p 184

Erkamp R, Wiggins P, Skovoroda A, Emelianov S and O'Donnell M 1998 Measuring the elastic modulus of small tissue samples *Ultrason. Imaging* **20** 17–28

Golub G and van Loan C 1996 *Matrix Computations* 3rd edn (Baltimore, MD: The Johns Hopkins University Press)

Hansen P 1998 *Rank-deficient and Discrete Ill-posed Problems* (Philadelphia, PA: SIAM)

Kallel F and Bertrand M 1996 Tissue elasticity reconstruction using linear perturbation method *IEEE Trans. Med. Imaging* **15** 299–313

Manduca A, Muthupillai R, Rossman P, Greenlead J and Ehman R 1996 Image processing for magnetic resonance elastography *Proc. SPIE* **2710** 616–23

Morozov V 1984 *Methods for Solving Incorrectly Posed Problems* (New York: Springer)

Ophir J, Kallel F, Varghese T, Bertrand M, Cespedes I and Ponnekanti H 1997 Elastography: a systems approach *Int. J. Imaging Syst. Tech.* **8** 89–103

Pelc N, Herfkens R, Shimakawa A and Enzmann D 1991 Phase contrast cine magnetic resonance imaging *Magn. Reson. Q.* **7** 229–54

Plewes D, Bishop J, Samani A and Sciarretta J 2000 Visualization and quantification of breast cancer biomechanical properties with magnetic resonance elastography *Phys. Med. Biol.* **45** 1591–610

Sarvazyan A *et al* 1994 Elasticity imaging as a new modality of medical imaging for cancer detection *Proc. Int. Workshop on Interaction of Ultrasound with Biological Media (Valenciennes, France)* pp 69–81

Sinkus R, Lorenzen J, Schrader D, Lorenzen M, Dargatz M and Holz D 2000 High-resolution tensor MR elastography for breast tumour detection *Phys. Med. Biol.* **45** 1649–64

Skovoroda A, Emelianov S, Lubinski M, Sarvazyan A and O'Donnell M 1994 Theoretical analysis and verification of ultrasound displacement and strain imaging *IEEE Trans. Ultrason. Ferroelectr. Freq. Control* **41** 302–13

Skovoroda A, Emelianov S and O'Donnell M 1995 Tissue elasticity reconstruction based on ultrasonic displacement and strain images *IEEE Trans. Ultrason. Ferroelectr. Freq. Control* **42** 747–65

Skovoroda A, Lubinski M, Emelianov S and O'Donnell M 1999 Reconstructive elasticity imaging for large deformations *IEEE Trans. Ultrason. Ferroelectr. Freq. Control* **46** 523–35

Steele D, Chenevert T, Skovoroda R and Emelianov S 2000 Three-dimensional static displacement, stimulated echo NMR elasticity imaging *Phys. Med. Biol.* **45** 1633–48

Weaver J, van Houten E, Miga M, Kennedy F, Hartov A, Poplack S, Nagy H and Paulsen K 1999 Measurement of harmonic motion for MR elastography *Proc. ISMRM, 7th Meeting (Philadelphia, PA)* p 1617